JGR Solid Earth

RESEARCH ARTICLE
10.1029/2023JB028514

Special Collection:
Advances in understanding volcanic processes

Branched Conduit Structure Beneath the Active Craters of Sakurajima Volcano Inferred From Muography

László Oláh[1,2], Gergő Hamar[1,2], Takao Ohminato[3], Hiroyuki K. M. Tanaka[2,3], and Dezső Varga[1,2]

[1]Institute for Particle and Nuclear Physics, HUN-REN Wigner Research Centre for Physics, Hungarian Research Network, Budapest, Hungary, [2]International Virtual Muography Institute, Tokyo, Japan, [3]Earthquake Research Institute, The University of Tokyo, Tokyo, Japan

Abstract Observing in-conduit physical mechanism underlying the switching of eruptive activity between the craters of multi-vent volcanoes could contribute to hazard assessment at these complex volcanic edifices. We performed monitoring of mass density changes beneath two active craters of Sakurajima volcano in Kyushu, Japan between September 2018 and July 2023 with cosmic-ray muography. From December 2022, the mass density decreased beneath Minamidake crater and increased beneath Showa crater in accordance with a switch of eruptive activity from Minamidake crater to Showa crater. Plug formation and convective magma degassing processes have been observed with muography in accordance with the deformation of the surface of volcanic edifice measured by Interferometric Synthetic Aperture Radar. We found a moderate inverse correlation with a Pearson's coefficient of −0.52 between the mass densities observed beneath the two active craters throughout the entire period. The inverse correlation of mass densities indicates a magmatic gas flux dynamics which characterizes a branched conduit structure. Muography thus reveals the shallow magmatic processes during switching of eruptive activity between the craters of multi-vent volcanoes and allows to infer to the conduit structure.

Plain Language Summary Observing the changing of structure and amount of materials in the upper plumbing systems of active volcanoes can contribute to the visualization the ongoing volcanic phenomena and assessing of related hazards. For instance, the increase in mass density indicates the uprise of deep volcanic materials in the conduit that may result in the onset of eruption. We measured the directional dependent yield of naturally occurring cosmic-ray muon particles across the active Sakurajima volcano in Kyushu, Japan. We utilized muography to visualize the changes in mass density structure beneath the erupting craters over time. The captured muon images revealed that the mass densities varied inversely underneath the Minamidake and Showa craters throughout the measurement period. The observed inverse correlation between the mass densities indicates a branched linkage between the conduits of the two active craters.

Key Points:

- Muography is utilized for visualizing and monitoring the mass density changes beneath the active craters of Sakurajima volcano, Kyushu, Japan
- Inverse correlation is found between the mass densities observed beneath the two active craters
- A branched linkage between the conduits of active craters inferred from the changes of eruptive activity and mass densities

Correspondence to:
L. Oláh,
olah.laszlo@wigner.hun-ren.hu

Citation:
Oláh, L., Hamar, G., Ohminato, T., Tanaka, H. K. M., & Varga, D. (2024). Branched conduit structure beneath the active craters of Sakurajima volcano inferred from muography. *Journal of Geophysical Research: Solid Earth*, *129*, e2023JB028514. https://doi.org/10.1029/2023JB028514

Received 9 DEC 2023
Accepted 9 SEP 2024

Author Contributions:
Conceptualization: László Oláh, Hiroyuki K. M. Tanaka
Formal analysis: László Oláh
Funding acquisition: László Oláh, Gergő Hamar, Takao Ohminato, Hiroyuki K. M. Tanaka, Dezső Varga
Investigation: László Oláh, Takao Ohminato, Hiroyuki K. M. Tanaka
Methodology: László Oláh
Project administration: László Oláh, Takao Ohminato, Hiroyuki K. M. Tanaka, Dezső Varga
Resources: László Oláh, Gergő Hamar, Takao Ohminato, Hiroyuki K. M. Tanaka, Dezső Varga
Software: László Oláh, Gergő Hamar
Visualization: László Oláh

1. Introduction

Multi-vent volcanoes are complex structures that change the location, style and intensity of eruptive activity. Consequently, hazard assessment is challenging at these volcanic edifices. Reconstructing the geometry of shallow plumbing system and localizing the sources of volcanic activity, linked to either magma migration at shallow depth within the conduit or the uprising of volatiles from a deep magma column, provide insights into the dynamics of multi-vent systems, specifically address why (Kahl et al., 2013) and how (Manga, 1996; Pioli et al., 2009) magma migrate between the vents. A linkage has been revealed between the conduits of Stromboli by thermal and infrasonic observations (Harris et al., 1996; Ripepe et al., 2007). Recently, spatiotemporal migration of vent locations has been observed by analyzing a database of infrared surveillance camera images. Salvatore et al. (2018) inferred that conduit geometry and vent shape control the explosion parameters and conduit branching controls the simultaneous versus alternating activity at shallow depths; while at larger depths, conduit geometry and location of the source of very long period seismic events control which vent erupts. Marchetti et al. (2009) found a strong evidence for gas partitioning and dynamics in an interconnected plumbing system of Mount Etna. The structural evolution of vents and the shifts of eruptive activity between the vents associated with changes in eruption mechanism (Zuccarello et al., 2022). In July 2014, Strombolian activity and lava effusion occurred in two adjacent vents of the eastern flank of Mount Etna (Spina et al., 2017). Here thermal analysis of eruption styles revealed a branched structure for the conduits and occurrence of rapid gas flux changes in the

Writing – original draft: László Oláh
Writing – review & editing: László Oláh, Hiroyuki K. M. Tanaka

inclined conduit. An interrelation has been revealed between the eruptive behavior of two craters of Yasur volcano, Vanuatu via statistical forecast modeling (Simons et al., 2020). The results of modeling enabled them to infer that the two conduits are separated at a deep magma reservoir and partitioning of magma and volatile flux in the complex plumbing system controls the eruptive behavior.

Tracking the movements and changes in the state of magma in multiple vents separated with a few tens of meters requires the application of geophysical monitoring techniques with sufficient spatial- and time resolutions. Infrasound microphones have been utilized for revealing infrasonic source locations beneath active craters of different volcanoes and recording signals created by magma degassing (e.g., Jones et al., 2008; Marchetti et al., 2009). Small-aperture seismic arrays have been applied for detecting volcanic tremors (e.g., Konstantinou & Schlindwein, 2002; Zuccarello et al., 2022). An integrated geophysical approach has been developed for tracking magma intrusion over space and time with an unprecedented resolution beneath the craters of Mount Etna (Cannavo et al., 2019). Recently, mechanical imaging via unsupervised learning of global navigation satellite system's data allowed to reconstruct magma migration at Piton de la Fournaise (Beauducel et al., 2020). In the present work, we aim to demonstrate the applicability of a developing geophysical observation technique, called muography, for exploring the conduit structures of multi-vent volcanic edifices the first time.

Muography allows passive, remote and high-resolution visualization and monitoring of mass density structure in solid, liquid and gas media (e.g., Oláh et al., 2022; Tanaka et al., 2023). A wide range of muography applications are under development (Tanaka et al., 2023) after pioneering works that focused on visualizing the internal structure of volcanoes (Nagamine et al., 1995; Tanaka, 2019; Tanaka et al., 2007) and exploring underground resources (Schouten & Lendru, 2018). Muography utilizes cosmic-ray muon particles originating from Earth's atmosphere from decaying of charged mesons that produced by collisions of primary cosmic-rays with the atmospheric atoms. The principle of muographic image processing is similar to conventional radiography (Tanaka et al., 2023): the flux of atmospheric muons is measured by particle detectors installed below the level of the structure to be imaged. The mass density-lengths (densities integrated along the path of muons, called also opacities in some works) are determined along the paths of penetrated muons via comparing the measured and simulated or modeled penetration rates of muons. Tomograpic inversion of multi-directional muographic image data (e.g., Nagahara et al., 2022; Tanaka et al., 2010) or joint inversion of muographic and gravimetric data (e.g., Cosburn et al., 2023; Gibert et al., 2022; Nishiyama et al., 2014) allow to reconstruct three-dimensional density structure in volcanic edifices with a few tens of meters spatial resolution. Various structural features and occurrence of volcanic phenomena have already been captured and studied with muon imaging in different volcanic edifices, for example, hydrothermal processes (Gibert et al., 2022), explosive eruptions (Oláh et al., 2023; Tanaka et al., 2014), investigation of lava dome formation processes and inspection of lava dome stability (Nagahara et al., 2022; Nishiyama et al., 2014; Portal et al., 2013; Tanaka, 2019), crater and conduit structures (Macedonio et al., 2022; Oláh, Tanaka, Ohminato, et al., 2019; Oláh et al., 2018; Tanaka, 2019; Tioukov et al., 2022), tectonic variations (Lo Presti et al., 2022), hydrogeomorphic changes due to tephra deposition (Tanaka, 2020), erosion and lahars (Oláh et al., 2021).

We apply a Multi-Wire Proportional Chamber-based Muographic Observation System (MMOS) for monitoring the mass density changes beneath the active craters of the Southern peak of Sakurajima volcano, Kyushu, Japan since 2017 (Oláh et al., 2018; Varga et al., 2020). Here the comparison of first muographic mass density images revealed magmatic plug formation underneath a deactivated crater (Oláh, Tanaka, Ohminato, et al., 2019). Recently, we utilized muography for complementing ground surface deformation monitoring and for explaining the link between eruption frequency and vertical uplifting of an active crater (Oláh et al., 2023). To our knowledge, the conduit structure has not yet been explored in Sakurajima volcano. Whether these are independent conduits which branch from the same reservoir or the conduit of Showa crater links to the conduit of Minamidake crater is an open question. In the present work, we aim to relate the time-sequential muographic images of the two active craters of Sakurajima volcano to the eruptive frequency and vertical uplifts of ground surface at these craters to investigate the structural linkage between the conduits.

2. Sakurajima Volcano

2.1. Geological Setting

The Sakurajima volcano is an andesitic stratovolcano that is fed with magma from the Aira caldera (Aramaki, 1984). Here the lithology has been characterized by the Geological Survey of Japan (2013). Eruptive

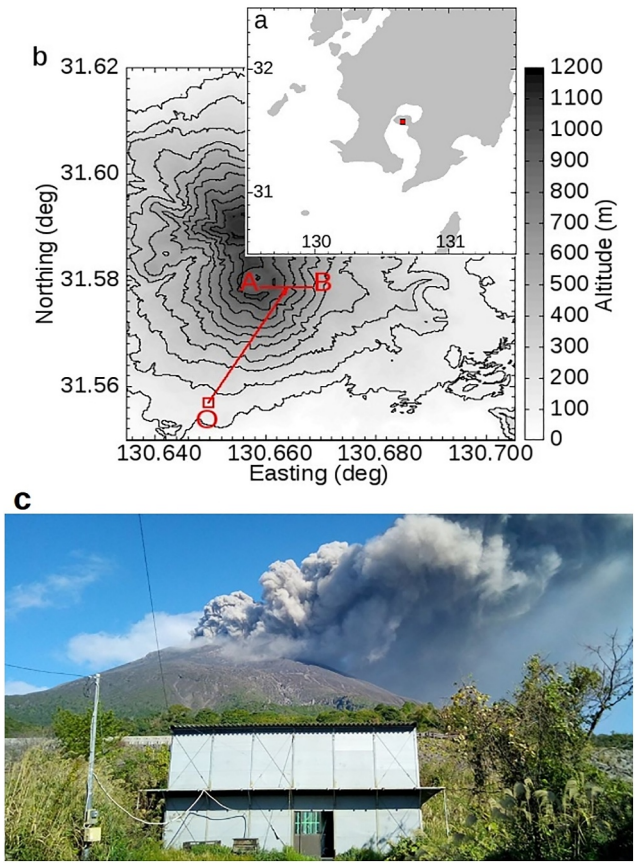

Figure 1. The measurement arrangement at Sakurajima volcano. (a) Map of south Kyushu, Japan is shown based on the data of Natural Earth (2024). A red-colored rectangle shows the location of measurement site. (b) The map of the measurement site is drawn based on the digital elevation data of Geospatial Information Authority of Japan (2023). The altitudes are shown relatively to the sea level. A red-colored rectangle shows the location of Sakurajima Muography Observatory (O) at latitude 31.557°N and longitude 130.650°E, at 150 m above sea level. Red arrow shows the azimuthal orientation of MMOS that was set to 30.25° from north. The MMOS was oriented horizontally. The AB line shows a selected cross-section across the crater region. (c) A photograph of the muography observatory is shown with the active southern peak of Sakurajima volcano in the background (Oláh & Tanaka, 2022).

activity occurs from two craters: the central crater of the southern peak, called Minamidake; and an auxiliary crater formed on the eastern flank of the southern peak at an altitude of 750 m above sea level (ASL) in 1939, called Showa crater. Minamidake and Showa craters are at elevations of 665 m ASL and 700 m ASL respectively, and separated horizontally by 500 m. Ground surface deformation measurements have been localized a magma chamber underneath the Aira caldera (Ishihara, 1990) and a shallow reservoir beneath the Southern peak (Uhira & Takeo, 1994). A three-pressure-source model suggested a deflation source beneath the Minamidake at 700 m below sea level that feeds the two active craters with magma (Hotta et al., 2016). Conduit size has been estimated to 40–60 m beneath the Showa crater by analyzing infra-sound and video records (Muramatsu et al., 2018).

2.2. Eruptive Activity

The eruptive activity alternates between the two active craters. During the studied period (from September 2018 to July 2023) the Minamidake and Showa erupted 1308 and 30 times, respectively. The eruptions are dominantly vulcanian type at both crater (Iguchi et al., 2008; Yokoo et al., 2013). Here the model of vulcanian eruptions infers the presence of magmatic plugs at the top of conduits, which beneath pressurized pockets of gas accumulate; and a failure of these cap rocks trigger the eruptions (Gabellini et al., 2022; Iguchi et al., 2008; Kazahaya et al., 2016; Oláh et al., 2023; Yokoo et al., 2013). The magnitude of Showa crater's eruptions are estimated to 10–100 times smaller than the magnitude of Minamidake crater's eruptions in the viewpoint of mass of ejected ash and various monitoring signals (Iguchi et al., 2013).

3. Instrumentation

Oláh et al. (2018), Oláh, Tanaka, Hamar, and Varga (2019), Oláh, Tanaka, Ohminato, et al. (2019), Oláh, Balogh, et al. (2019), Oláh et al. (2021), Oláh and Tanaka (2022), and Oláh et al. (2023) described the experimental setting and data acquisition at Sakurajima volcano, Kyushu, Japan (Figure 1a). Here we present the MMOS in nutshell as follows. This is a modular muographic observation system that is constructed from gaseous tracking detectors (Oláh et al., 2018, 2021; Varga et al., 2020, 2022). It consists of 11 tracking systems that are installed at the same location in Sakurajima Muography Observatory (SMO) at latitude 31.557°N and longitude 130.650°E, at altitude 150 m ASL (empty red-colored rectangle in Figure 1b). The distance of SMO is about 2.8 km from the active craters of Sakurajima volcano. The main axis of MMOS detector is horizontal with the azimuth of 30.25° from north (red arrow on Figure 1b). The detector is assembled from vertical modules. The 0 of directional tangents tan (θx) and tan (θy) coincide with the axis direction.

Figures 2a and 2b show a photograph and schematic drawing about a typical assembling of an MMOS module. A module consists of seven or eight Multi-Wire Proportional Chambers (MWPCs) that are installed along a length of 2 m (Nyitrai et al., 2021; Varga et al., 2016). The MWPC is a 20-mm-thick gaseous detector in which a measurable signal (a few tens of thousands electrons) is created via ionization of Ar gas atoms by the penetrating charged particles. The MWPCs are equipped with three types of wires in two perpendicularly oriented wire planes: (a) an upper wire plane where 20–25 μm-diameter gold-plated tungsten anode wires are used for gas amplification and 100-μm-diameter copper wires are used between the anode wires for electric field shaping; and (b) a lower wire plane where 100-μm-thick copper wires are used for picking-up the signals (Varga et al., 2016). An 1,750–1,775 V high-voltage is supplied to the anode wires to create an electric field in the detector volume to induce electron avalanches. Other wires are on ground potential. All anode wires are connected together to provide a common analog signal for triggering and gas amplification measurements. The wire spacing is set for 12 mm for both wire planes. This construction allows a 1 + 1-dimensional position measurement for each MWPC.

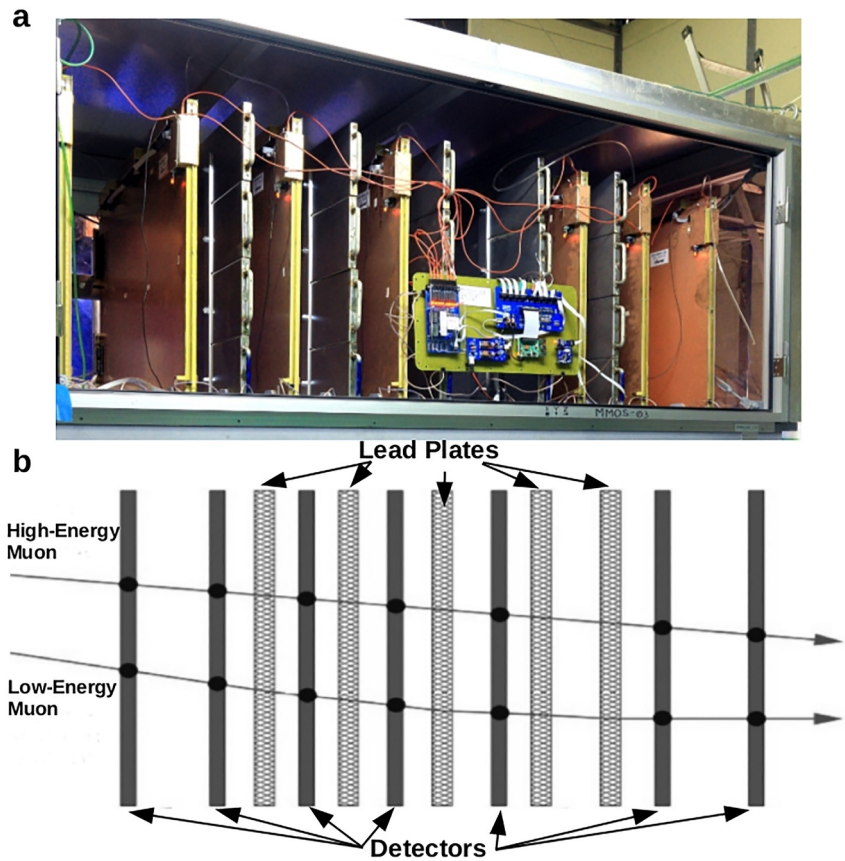

Figure 2. Structure of muon tracking system. (a) Photograph about an MMOS module which consists of seven MWPC detectors and five 2-cm-thick lead plates (Oláh, Tanaka, Ohminato, et al., 2019). (b) 1-dimensional schematic drawing of a typical detector assembly from MWPCs and lead plates. High-energy muons and low-energy muons penetrate across the tracking system with negligible and significant deflections, respectively. The deflection is quantified on track-by-track basis with the goodness of linear fit performed on the measured cluster centroids.

The positional resolution has been measured to about 4 mm in both dimension for each MWPC in this setup (Oláh et al., 2018; Varga et al., 2016). The angular resolution of the MMOS approaches 3 mrad that is close to the physical upper limit (Oláh, Tanaka, Hamar, & Varga, 2019; Oláh et al., 2018). Five 20-mm-thick lead plates coated with stainless steel are installed between the MWPCs (Figure 2b) for deflecting or absorbing the low-energy (<1 GeV) background particles that are mostly muons and other components of cosmic-rays which did not penetrate the volcano (Ambrosino et al., 2015; Nishiyama et al., 2016).

Custom designed electronics are applied for amplifying and discriminating the electric signals acquired from the position sensitive field-shaping and pick-up wires (Varga et al., 2020, 2022). Data collection is triggered by a coincidence of three or more MWPCs. The data collection and detector operation are controlled by microcomputers in each MMOS module. The trigger is blocked during the data readout that results in a dead time of about 300 microseconds per event. The data recorded event-by-event. ASCII files are closed and compressed and a new file is opened after a few hours. All modules are communicating with a local server microcomputer. The local server allows simultaneous detector control, data management and time synchronization of different modules (Varga et al., 2020). The compressed data files are copied to a remote computer where monitoring of operational performance and data quality assurance are performed by automated software.

Power supplying of MMOS is provided by local electricity network. Uninterruptible power supplies and +12V DC batteries allow continuous operation during short (less than few hours duration) power cuts that occur during typhoon season (August–October). A cluster of six gas bottles filled with Ar-CO_2 gas mixture (80%:20%) supplies the MMOS. Each gas bottle has a volume of 40 L and a filling pressure of 150 bar. The gas flow rate is set to

about 1 L per hour. A set of six gas bottles allows continuous operation for 4 months (Nyitrai et al., 2021; Varga et al., 2020).

4. Data Collection

4.1. Muographic Data

The MMOS system continuously acquired data from 1 September 2018 to 1 July 2023, except when we stopped it for a few days biannual for installing of new tracking systems and conducting maintenance or replacement of malfunctioned detector elements. The event-by-event data include has the following structure: a time stamp, a time difference in microseconds relative to previous event, particle hit coordinates for each MWPC, analog signal amplitudes for each MWPC, a trigger pattern, high-voltage and current data, as well as temperature-humidity-pressure sensor data (Oláh, Tanaka, Hamar, & Varga, 2019; Varga et al., 2020). Off-line data quality assurance (Section 5) has been conducted to remove the low-quality data for periods when the track rates and detection efficiencies decreased significantly due to temporary malfunctioning of different elements of MMOS modules (electronics, MWPCs, etc.). Furthermore, data collection has been stopped during maintenance of MMOS system and installation of new MMOS modules. Monthly data about the operational periods of MMOS modules have been published in a data base of Open Science Framework (Oláh, 2024a).

4.2. Interferometric Synthetic Aperture Radar (InSAR) Data

Ground deformation monitoring have been performed simultaneously with muographic observation. Vertical displacements of volcano's surface have been determined with 12 days periodic time via analyzing the Phased Array type C-band Synthetic Aperture Radar images acquired with Sentinel-1 satellite (The European Space Agency, 2023). NEC Corporation analyzed the InSAR images independently from our analysis (Oláh et al., 2023). They quantified the vertical displacements relatively to the ground levels determined for 31 October 2018 and 6 April 2021, respectively.

5. Methodology

Off-line analysis of muographic data has been conducted. These methods have been presented in our earlier works (Oláh, 2024b; Oláh, Balogh, et al., 2019; Oláh & Tanaka, 2022; Oláh, Tanaka, Hamar, & Varga, 2019; Oláh, Tanaka, Ohminato, et al., 2019; Oláh et al., 2021). In the present work, the relevant output of data analysis is the mass density image. Each muographic image use the natural coordinate system of the MMOS that is based on the tangents of horizontal- and elevational angles (slopes of track projections) measured respect to the detector orientation: tan (θx) and tan (θy). Each density image has 33×33 pixels (angular bins) with a size of 0.023 in both horizontal and vertical directions. Each pixel corresponds to an area of approx. 60 m × 60 m at the craters. Each image is determined for a period of 6 months for this study. The main procedures of the analysis chain are presented in the following subsections.

5.1. Track Reconstruction and Track Selection

Track reconstruction and selection are conducted independently for the horizontal and vertical directions for each tracking system (Oláh et al., 2018). This method initiates with reconstructing the centroids, sizes and number of particle hit clusters in each MWPC. The cluster sizes were measured to two or three in both wire plane. The number of clusters was found between one and three for events without electronic noise. MWPCs with either large number (>5) or large size (>6) clusters are excluded from the track fitting to avoid biasing the slope of reconstructed track. This analysis allows the loss of one MPWC before constructing track candidates. The cluster centroid coordinates are gathered into track candidates and fitted with straight lines. The slopes, intersects and goodness of fit (chi square divided by the number of degrees of freedom) parameters were calculated for each line. The chi square is defined as follows.

$$\chi^2 = \Sigma_{i=1:N\mathrm{det}} \left[\left(C_{\mathrm{measured},i} - C_{\mathrm{fitted},i} \right)^2 / \sigma^2 \mathrm{det},i \right], \quad (1)$$

where $C_{\mathrm{measured},i}$ is the reconstructed cluster centroids, $C_{\mathrm{fitted},i}$ is the intersection of the fitted straight track on the given detector layer, $\sigma\mathrm{det},i \approx \sigma\mathrm{MWPC}$ is the position resolution of the MWPCs, and $N\mathrm{det}$ is the number of

MWPCs. The number of degrees of freedom equals to the number of MWPCs minus 2 for each direction of the tracking system. The energy cut is set to reject at least 90% of muons with energies below 1 GeV. This cut have been determined by simulating the penetration of muons across the tracking system in GEANT4 framework (Agostinelli et al., 2003) and reconstructing them by the same tracking algorithm that reconstructs the experimental data (Oláh & Tanaka, 2022; Oláh, Tanaka, Hamar, & Varga, 2019). The value of chi square cut varies between 1.5 and 2.5 for the different tracking systems. Application of this cut resulted in a 2.5% loss of muons at few GeVs energies (Oláh, Tanaka, Ohminato, et al., 2019).

5.2. Detector Calibration and Detection Efficiency

Distribution of differences between the measured cluster centroids and fitted line coordinates are measured for each MWPC. The average values of these residual distributions quantify the misalignments of detector layers. The calculated misalignments are added to the reconstructed cluster centroids in the cluster reconstruction algorithm to align the MWPCs. The hits are measured for each channel. Channels are defined to noisy if the number of hits are found five times larger than the average hits of all channels. Noisy channels are excluded from further analysis.

The tracking and triggering efficiencies are quantified by a combinatorial algorithm. Here the investigated MWPC is excluded. A tracklet is constructed from the clusters measured on the other MWPCs. The tracklet is extrapolated to the investigated MWPC and the presence of a cluster is checked within a fiducial region (±2 channels) of the extrapolated coordinate. Tracking efficiency is determined by the number of found clusters divided by the number of extrapolations. The trigger efficiency is given by the number of tracklets when the investigated MWPC provides a trigger signal divided by the number of extrapolations. The tracking and trigger efficiency are measured for each MWPC above 90% and 95%, respectively.

The aforementioned dead time is quantified by determining the time difference value where the distribution of time differences between the consecutive recorded triggers exceeded zero. The dead time results in a <0.1% loss of muons for each tracking system.

5.3. Muon Flux Calculation

The flux calculation is conducted independently for each MMOS module in the above defined angular binning. The flux is calculated for each slope bin as follows.

$$F = N / [A \times \Omega \times t], \tag{2}$$

where N is the number of tracks, A is the detection surface, Ω is the covered solid angle, t is the data collection time. The calculated fluxes are merged by taking into account the horizontal orientation of tracking systems. The procedure determines the muon fluxes with an angular binning of 0.006 and extracted the horizontal rotation of each tracking system where the flux difference has a minimum relative to a reference tracking system. An example has been presented for this procedure by Oláh, Balogh, et al. (2019). The corrections have been found below 0.012 for each tracking system. Figures 3a–3c show respectively the path-lengths that have been calculated using the digital elevation model data of volcanic edifice (Geospatial Information Authority of Japan, 2023), the muon track counts and the calculated muon flux in the natural coordinate system of MMOS for a period from 1 December 2022 to 31 May 2023. These figures show that the MMOS system collected sufficient number of muons across thickness below 2.5 km during an observation period.

5.4. Forward Modeling of the Muographic Data

The averaged mass density values are determined for each angular bin via minimizing the difference between the measured and forward modeled muon fluxes. The forward modeling of muons fluxes are performed by integrating parametrized angular and energy dependent muon spectra (Tang et al., 2006) from a minimal energy of muons which can penetrate the volcano along their path (Groom et al., 2002). Figure 4 shows the parametrized muon fluxes (black lines) for selected zenith-angles. The colored dots show experimental data (Alkoffer et al., 1985; Jokisch et al., 1979) that validate the parametrization. The minimal energies have been determined by Monte Carlo simulations that taking into account accurately the radiative energy loss processes of high-energy muons (Lipari & Stanev, 1991). The penetration of muons have been simulated across silicon dioxide with a mass density

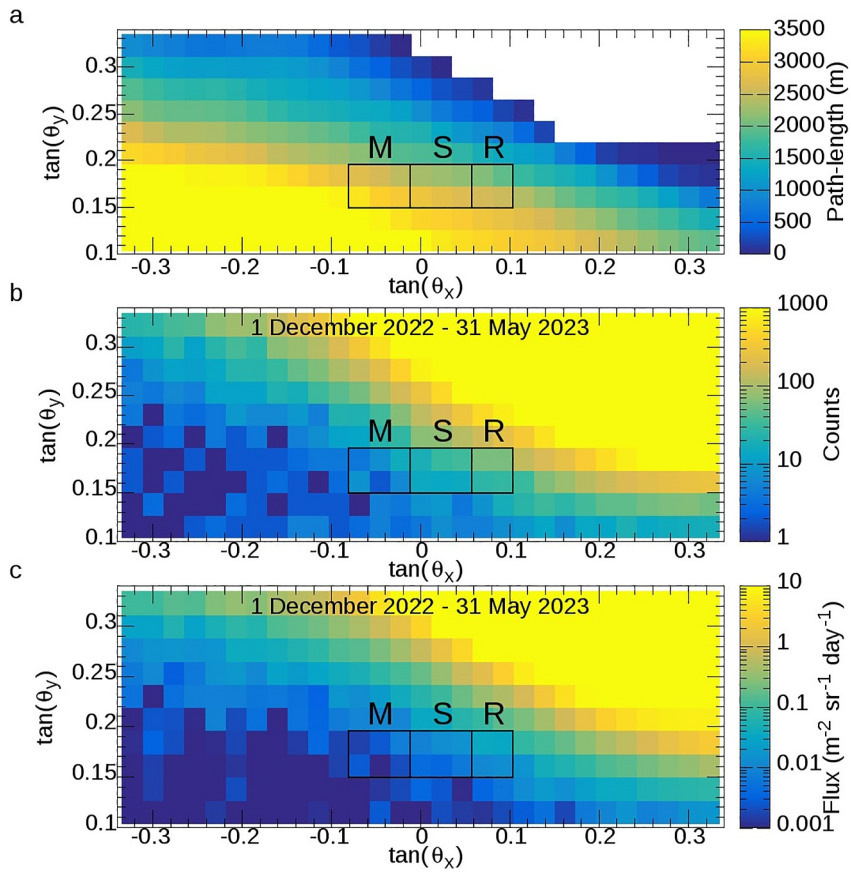

Figure 3. All quantities have been determined in natural coordinate system of the MMOS. Black rectangles highlights the studied regions beneath the Minamidake crater (*M*), Showa crater (*S*) and across a Reference region (*R*). (a) Path-lengths have been determined using the digital elevation model of the volcanic edifice. (b) The track counts measured across the crater region for the period from 1 December 2022 to 31 May 2023. (c) The measured muon flux values are shown for the same period.

of 2.1 g cm^{-3} and different thicknesses in GEANT4 framework (Agostinelli et al., 2003). The simulated data have been analyzed on event-by-event basis to determine the energy spectra of generated and penetrated muons. The energy minimum has been extracted at the energy value where the sum of generated muons was found equal with the number of penetrated muons. Figure 5 shows the minimum muon energies ($E_{\min}$) in MeV units as a function of penetrated density-lengths (X) in g cm^{-2} units for our GEANT4 simulation (black circles). The minimum energy was parametrized by a third order polynomial fit (black line): $E_{\min}(X)$ [MeV] = $p_1X + p_3X^3$, where $p_1 = 2.62 \pm 0.06$ MeV g^{-1} cm^2 and $p_3 = (165.98 \pm 1.88) \times 10^{-13}$ MeV g^{-3} cm^6.

6. Results

6.1. Time-Sequential Mass Density Images

Figures 6a–6x show the muographic density images with 45 pixels about the crater region from January 2021 to June 2023. The black line visualizes a slice of topography in the craters of southern peak along the AB line of Figure 1b. Black rectangles highlight three selected regions underneath the eastern part of Minamidake crater (*M*), underneath the Showa crater (*S*) and a Reference region (*R*) in which volcanism does not occur. The path-averaged densities (ρ) ranged from 0.9 to 1.8 g cm^{-3} through the regions *M* and *S*. The density values ranged from 0.95 to 1.05 g cm^{-3} through the region *R*. Here the lower densities are likely caused by the energetic (>1 GeV) background particles. These density images visualize how the mass densities changed over time through the regions beneath the eastern part of Minamidake crater and beneath Showa crater. The muographic images shows that the density increased beneath the Minamidake crater and decreased beneath the Showa crater after January 2022.

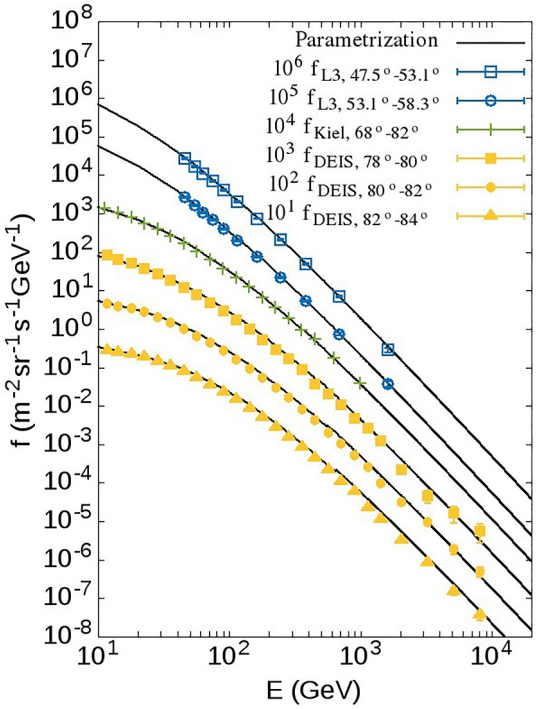

Figure 4. Forward modeling of muon flux. Energy and zenith-angle dependent muon spectra have been parametrized with a modified Gaisser model (Tang et al., 2006). Black lines show the parametrized muon spectra for selected zenith-angles. The colored dots show the experimental data for the same angular regions (Alkoffer et al., 1985; Jokisch et al., 1979).

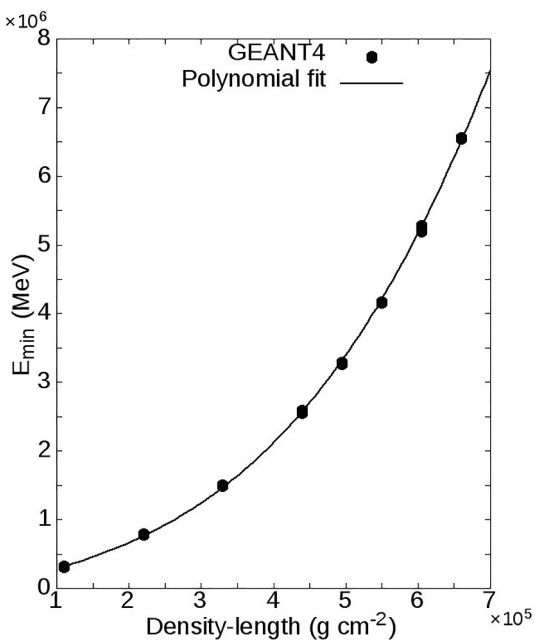

Figure 5. Simulated minimum energies are shown as a function of density-lengths for silicon dioxide (black circles). Black line shows a fitted third-order polynomial function (Oláh & Tanaka, 2022).

6.2. Mass Density Variation Across the Crater Region

Figures 7a–7c show the 6 month average (arithmetic mean values) of mass densities with one standard deviation for the regions *M*, *S*, and *R* (black dots with error bars) and the monthly number of eruptions (orange-colored histograms) from September 2018 to July 2023. The averaged density increased beneath the eastern part of Minamidake crater (Figure 7a) from January 2022 to July 2022 and decreased after the January 2023. The changes of average densities exceeded 0.25–0.3 g cm^{-3} which is significantly above the systematic density error of 0.06 g cm^{-3} (Oláh & Tanaka, 2022). Throughout the same period, densities decreased through region *S* (Figure 7b) when the densities increased through region *M*, and vice versa. The density increased underneath the Showa crater, whereas the density decreased through the conduit of Minamidake from December 2022. After switching in trends of mass density changes, the Showa crater activated in January 2023 (orange-colored histogram in Figure 7b). The density changes were found below 0.1 g cm^{-3} through the Reference region (Figure 7c) during the entire observation period.

6.3. Anti-Correlation of Mass Densities

Figure 8 shows a scatter plot for the mass densities measured beneath the eastern part of Minamidake crater and Showa crater from September 2018 to July 2023. The Pearson's coefficient was quantified to −0.52 for these mass density values. It is worth noting that while the mass density beneath Showa is anti-correlated with the mass density beneath Minamidake, the InSAR data at Showa has a similar trend to the InSAR data at Minamidake. The ground deformation is observed as an indirect response to a deep deformation source, thus the regions where the volcanic edifice uplifted are not localized within the size of the deformation source. Although muography can not detect deep density variations, it is sensitive to more localized mass density changes and movements inside the volcanic edifice.

7. Discussion

7.1. Linkage Between the Active Craters

Figures 6o–6y shows that the conduits are unified beneath the eastern part of Minamidake crater and Showa crater and this unified volume might be slanted toward east. Other monitoring signals also indicate the link between the active craters: The seismic epicenters distributed beneath both craters at shallow depths from September to December 2020 and June to December 2021 (Japan Meteorological Agency, 2021) when densities increased across the region *M* and *S*, respectively. Infrared thermal imaging revealed simultaneous presence of geothermal areas in the eastern part of Minamidake crater and Showa crater in October 2021 (Japan Meteorological Agency, 2021), in February and October 2022 (Japan Meteorological Agency, 2022). The eruptive activity has switched from Minamidake crater to Showa crater in June 2023 (Japan Meteorological Agency, 2023).

7.2. Plug Formation

Figure 7a shows increasing mass densities beneath Minamidake crater before the onset of eruptions at Minamidake crater and decreasing mass densities beneath Minamidake crater during the eruptions at Minamidake crater. This trend is consistent with our earlier observations on Minamidake crater (Oláh et al., 2023). The increasing trend is interpreted as plug formation due to magma rising. The decreasing trend is interpreted as plug reduction due to

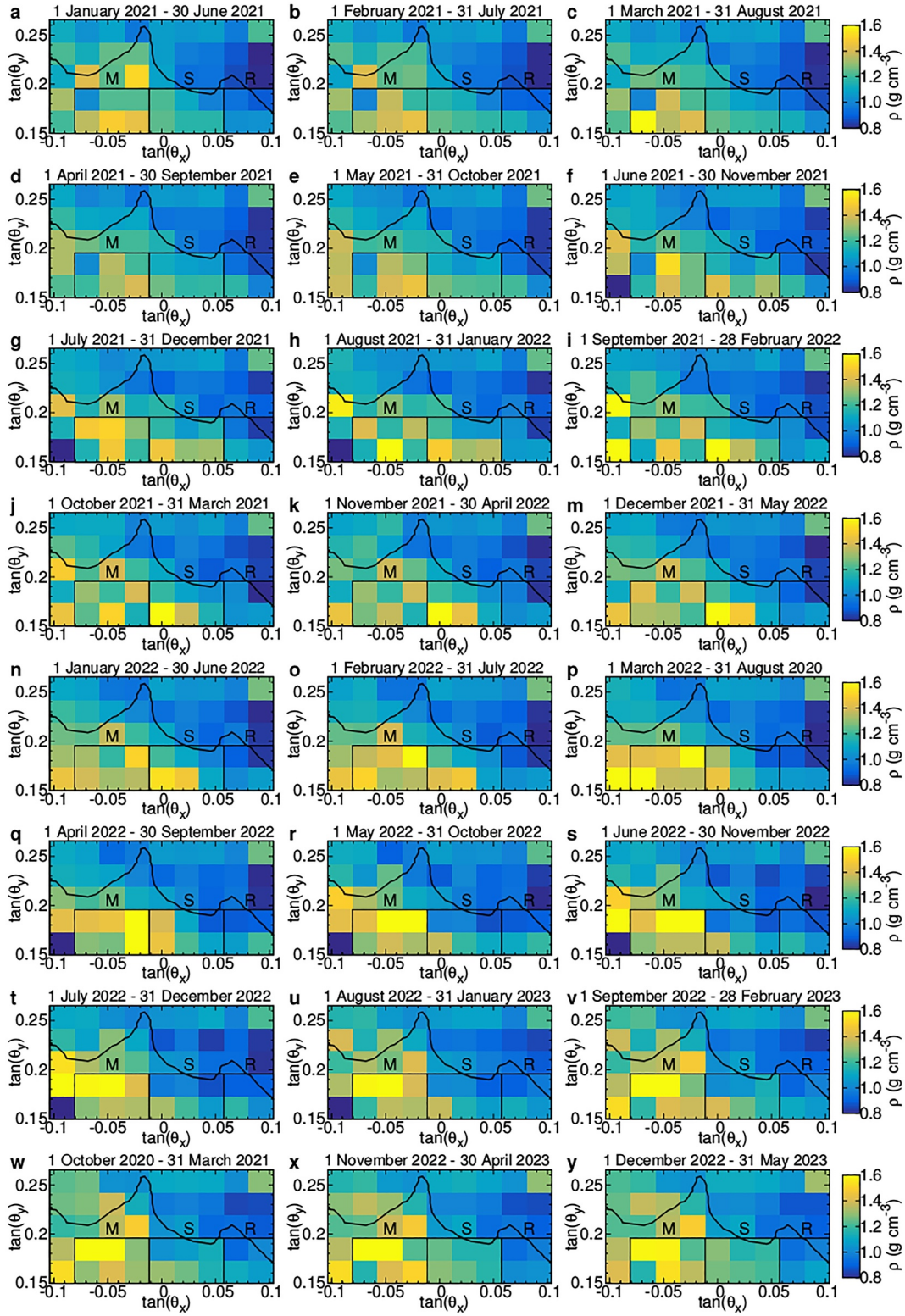

Figure 6. Time-sequential density images of Sakurajima volcano. (a–y) The average densities (ρ) are plotted for the crater region as a function of horizontal and elevation directions for periods of 6 months from 1 January 2021 to 31 May 2023. The densities were calculated for angular bins with the size of $\Delta\tan(\theta x) \times \Delta\tan(\theta y) = 0.023 \times 0.023$ each. Black lines show the cross-section of craters along the AB line of Figure 1a. Black rectangles show designated regions beneath the Minamidake crater (M), the Showa crater (S) and the Reference region (R), respectively.

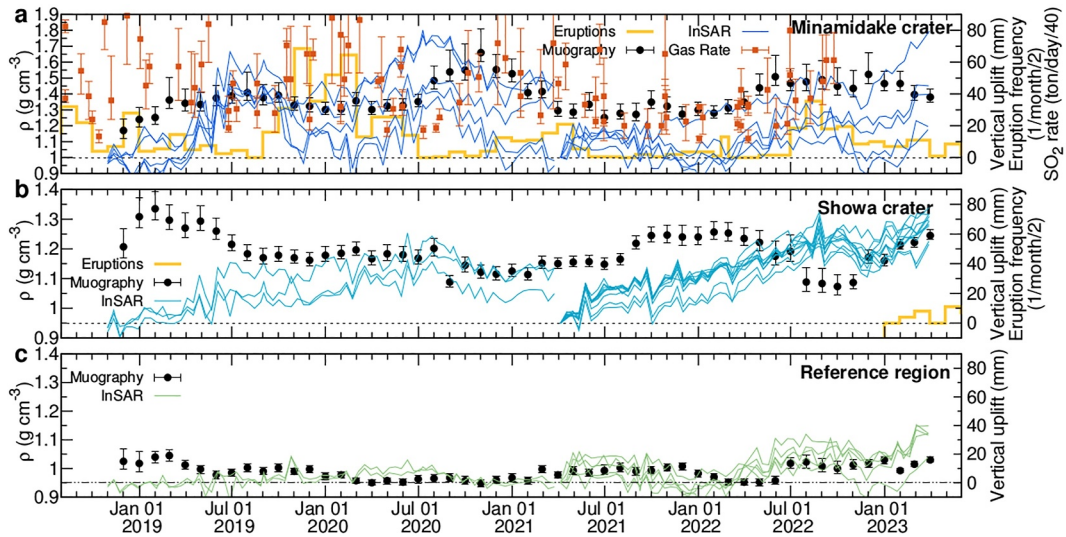

Figure 7. Time evolution of averaged densities through the three regions of Sakurajima volcano. The densities (black dots) are shown with 1 standard deviation error bars from September 2018 to July 2023. The dots refer to the mids of time intervals. The colored lines show vertical uplifts quantified from ground deformation data measured by InSAR (Oláh et al., 2023). (a) Averaged densities are shown for the region beneath the Minamidake crater. The eruption frequency of Minamidake crater is shown by the orange histogram. The SO_2 emission rates are shown with brown-colored rectangles with error bars (Japan Meteorological Agency, 2022). (b) The average densities are shown for the region beneath the Showa crater. The eruption frequency of Showa crater is shown by the orange histogram. (c) Average densities are shown for the Reference region.

recurrent eruptions. The InSAR data and SO_2 flux data (Japan Meteorological Agency, 2022) support this picture. The magma has recurrently risen and the plug was recurrently generated underneath both of the craters. However, at Minamidake crater, sufficient gas was provided and as a result, the gas pressure has risen. Consequently, the ground surface was significantly upheaved in the Minamidake crater region. The SO_2 flux (brown-colored rectangles) correlated with the mass densities during the measurement period which suggest that mass density increased within the conduit occurred as a response of magma degassing.

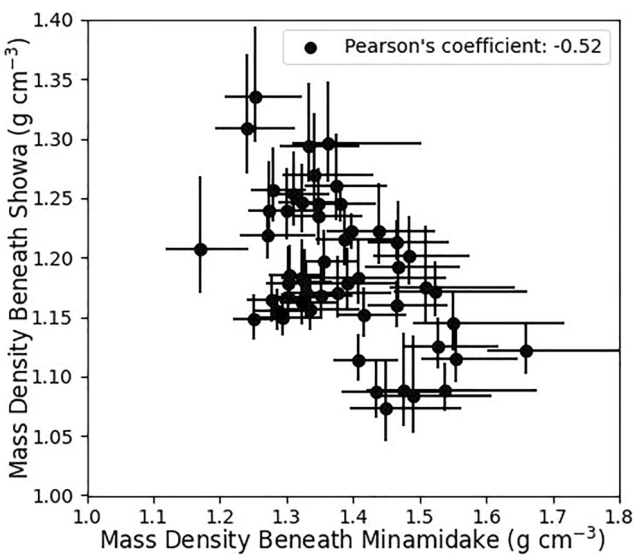

Figure 8. Scatter plot of mass density values measured beneath the Minamidake and Showa craters. The Pearson's coefficient was found to −0.52 that indicates a moderate anti-correlation between the mass densities.

7.3. Convective Magma Degassing

On the contrary, Figure 7b shows that eruptions did not follow the density increase observed beneath Showa crater in January 2019 and in August 2021; however, later the mass density decreased. It was interpreted that the uprising magma generated the plug underneath Showa crater. However, the gas pressure mightn't be enough to trigger eruptions. Convective magma degassing occurred within the conduit (Miyagi et al., 2013 and references therein) that induced bubble formation which decreased the mass density in this region. The InSAR data acquired at Showa crater showed that sufficient gas was not provided after the plug formation underneath Showa crater, thus the ground surface was not significantly upheaved. Furthermore, the SO_2 flux (brown-colored rectangles in Figure 7a) was measured above 2000 tons per day from July 2018 to June 2019 and in August 2021 (Japan Meteorological Agency, 2022). It is worth noting that the currently the gas flux is measured for both craters. On the contrary, in February 2023, from the InSAR data, there was an indication that the pressure underneath the generated magmatic plug increased underneath Showa crater, inducing a significant uplift of the ground surface in the Showa crater region. Consequently eruption occurred at Showa crater.

7.4. Branched Conduit Structure Inferred From Inverse Correlation of Mass Densities

As shown in Figure 8, it was indicated that there was a moderate anti-correlation between the mass densities measured underneath Minamidake crater and Showa crater for the period from September 2018 to June 2023. The Pearson's coefficient was found to −0.52. Infrasonic monitoring data showed a similar anti-correlation between the regions beneath the adjacent craters of Mount Etna. Marchetti et al. (2009) observed the switching of infrasonic source locations and change of activity between the Bocca Nuova and the South East Crater (SEC). Their infrasonic source measurements indicated that the pressure of multi-phase magma mixture in the conduits increased either in Bocca Nuova or SEC, but it had never increased in both of the craters at the same time. Spina et al. (2017) and Zuccarello et al. (2022) observed similar trends in thermal and tremor data, respectively. It was inferred that the summit craters represented the preferential pathway of degassing.

Likewise, it was also inferred that the summit craters of Sakurajima Volcano represented the preferential pathway of degassing based on our findings: an anti-correlation between the mass densities measured underneath Minamidake crater and Showa crater. As was discussed in the prior work (Oláh et al., 2023), the changes in the muographically measured mass densities represent the changes in the pressure of magmatic gas beneath the plug located at the top of the conduit. The switching of eruptive activity occurred from Minamidake crater to Showa crater when the mass density and vertical uplift exceeded a local maximum at Minamidake before January 2023 (Figure 6a, where the uplifts are shown relatively to a value quantified for 6 April 2021 after this date). Thereafter, the mass densities decreased beneath Minamidake crater and increased beneath Show crater in accordance with the inverse correlation observed for the entire period, suggesting that magma degassing occurs either in Minamidake crater and in Showa crater, acting as a similar preferential pathway to the one observed in Etna. Consequently, it was concluded that there is also a similar branched conduit system at Sakurajima volcano with a nearly vertical conduit for the Minamidake crater and a connecting slant vent for the Showa crater.

8. Conclusions

We performed mass density monitoring across a shallow (120–180 m) region beneath the active craters of Sakurajima volcano with muography. We inferred to plug formation and drained-back processes beneath the active craters from the muography. Ground deformation monitoring has also been performed on the volcanic edifice and changes in vertical uplifts over time supported the muographic observations. This implies that time-sequential muography of mass density changes through the upper conduits of adjacent craters can be applied for studying the dynamics of shallow magmatic processes during the switch of eruptive activity between the craters.

Muography does not allow us to explore the deeper parts of the conduit because the density-length range of muography is limited due to the small number of muons which have sufficient energy to penetrate beyond a few kilometers in rock. However, studying the relation between the mass densities measured beneath the adjacent craters with muography allowed us to infer to the structure of the plumbing system the first time to our knowledge. Beneath the active craters of Sakurajima volcano, a branched conduit structure was inferred from the inversely correlated mass densities. To our knowledge, this represents a new contribution to the understanding of the shallow conduit structure at Sakurajima volcano.

Mass density monitoring with muography maybe applicable for studying the shallow parts of other multi-vent volcanoes where eruption mechanism is assumed to be similar (e.g., Burgisser et al., 2011; Iguchi et al., 2008; Watt et al., 2007).

Data Availability Statement

The data sets and software of this study are available in a data repository in Oláh (2024a, 2024b).

Acknowledgments

This work was supported by the Ministry of Education, Culture, Sports, Science and Technology, Japan (MEXT) Integrated Program for the Next Generation Volcano Research, the Joint Usage Research Project (JURP) of the University of Tokyo, Earthquake Research Institute, University of Tokyo (ERI) under project ID 2023-H-03, the Hungarian NKFIH research grants under identification numbers OTKA-FK-135349, TKP2021-NKTA-10, the HUN-REN Welcome Home and Foreign Researcher Recruitment Programme KSZF-144/2023; and the "INTENSE" H2020 MSCA RISE, GA No. 822185. Detector construction and testing was completed within the Vesztergombi Laboratory for High Energy Physics (VLAB) at Wigner RCP. The technical support provided by the members of the REGARD group is gratefully acknowledged. We thank the useful discussions to Masato Iguchi, Isoji Miyagi and Edward W. Llewellin.

References

Agostinelli, S., Allison, J., Amako, K., Apostolakis, J., Araujo, H., Arce, P., et al. (2003). GEANT4–A simulation toolkit. *Nuclear Instruments and Methods in Physics Research*, *506*(3), 250–303. https://doi.org/10.1016/S0168-9002(03)01368-8

Alkoffer, A. C., Jokisch, H., Klemke, G., Oren, Y., Uhr, R., Bella, G., et al. (1985). Cosmic ray muon spectra at sea-level up to 10 TeV. *Nuclear Physics B*, *259*, 1–18. https://doi.org/10.1016/0550-3213(85)90294-9

Ambrosino, F., Anastasio, A., Bross, A., Béné, S., Boivin, P., Bonechi, L., et al. (2015). Joint measurement of the atmospheric muon flux through the Puy de Dôme volcano with plastic scintillators and Resistive Plate Chambers detectors. *Journal of Geophysical Research: Solid Earth*, *120*(11), 7290–7307. https://doi.org/10.1002/2015jb011969

Aramaki, S. (1984). Formation of the Aira Caldera, southern Kyushu, ~22,000 years ago. *Journal of Geophysical Research: Solid Earth*, *89*(B10), 8485–8501. https://doi.org/10.1029/JB089iB10p08485

Beauducel, F., Peltier, A., Villie, A., & Suryanto, W. (2020). Mechanical imaging of a volcano plumbing system from GNSS unsupervised modeling. *Geophysical Research Letters*, *47*(17), e2020GL089419. https://doi.org/10.1029/2020GL089419

Burgisser, A., Arbaret, L., Druitt, T. H., & Giachetti, T. (2011). Pre-explosive conduit conditions of the 1997 Vulcanian explosions at Soufrière Hills Volcano, Montserrat: II. Overpressure and depth distributions. *Journal of Volcanology and Geothermal Research*, *199*(3–4), 193–205. https://doi.org/10.1016/j.jvolgeores.2010.04.008

Cannavo, F., Sciotto, M., Cannata, A., & Di Grazia, G. (2019). An integrated geophysical approach to track magma intrusion: The 2018 Christmas Eve eruption at Mount Etna. *Geophysical Research Letters*, *46*(14), 8009–8017. https://doi.org/10.1029/2019GL083120

Cosburn, K., Roy, M., & Nishiyama, R. (2023). A machine learning approach to joint gravity and cosmic-ray muon inversion at Mt. Usu. *Geophysical Journal International*, *233*(2), 1081–1096. https://doi.org/10.1093/gji/ggac497

Gabellini, P., Cioni, R., Geshi, N., Pistolesi, M., Miwa, T., Lacanna, G., & Ripepe, M. (2022). Eruptive dynamics and fragmentation mechanisms during cyclic Vulcanian activity at Sakurajima volcano (Japan): Insights from ash texture analysis. *Journal of Volcanology and Geothermal Research*, *428*, 107582. https://doi.org/10.1016/j.jvolgeores.2022.107582

Geological Survey of Japan. (2013). Geological map of Sakurajima volcano. Retrieved from https://gbank.gsj.jp/volcano/ActVol/sakurajima/text/eng/exp01-1e.html

Geospatial Information Authority of Japan. (2023). GSI home page. Retrieved from http://www.gsi.go.jp/

Gibert, D., de Bremond d'Ars, J., Carlus, B., Deroussi, S., Ianigro, J., Jessop, D. E., et al. (2022). Observation of the dynamics of hydrothermal activity in La Soufrière of Guadeloupe volcano with joint muography, gravimetry, electrical resistivity tomography, seismic and temperature monitoring. *Geophysical Monograph Series*, *270*, 55–73. https://doi.org/10.1002/9781119722748.ch5

Groom, D. E., Mokhov, N. V., & Striganov, S. I. (2002). Muon stopping power and range tables 10 MeV-100 TeV. *Atomic Data and Nuclear Data Tables*, *76*(2), 183–356. https://doi.org/10.1006/adnd.2001.0861

Harris, A. J. L., Stevens, N. F., Maciejewski, A. J. H., & Rollin, P. J. (1996). Thermal evidence for linked vents at Stromboli. *Acta Vulcanologica*, *8*, 57–61.

Hotta, K., Iguchi, M., Ohkura, T., & Yamamoto, K. (2016). Multiple-pressure-source model for ground inflation during the period of high explosivity at Sakurajima volcano, Japan—Combination analysis of continuous GNSS, tilt and strain data. *Journal of Volcanology and Geothermal Research*, *310*, 12–25. https://doi.org/10.1016/j.jvolgeores.2015.11.017

Iguchi, M., Tameguri, T., Ohta, Y., Ueki, S., & Nakao, S. (2013). Characteristics of volcanic activity at Sakurajima volcano's Showa crater during the period 2006 to 2011. *Bulletin of the Volcanological Society of Japan*, *58*, 115–135. https://doi.org/10.18940/kazan.58.1_115

Iguchi, M., Yakiwara, H., Tameguri, T., Hendrasto, M., & Hirabayashi, J. (2008). Mechanism of explosive eruption revealed by geophysical observations at the Sakurajima, Suwanosejima and Semeru volcanoes. *Journal of Volcanology and Geothermal Research*, *178*, 1–9. https://doi.org/10.1016/j.jvolgeores.2007.10.010

Ishihara, K. (1990). Pressure sources and induced ground deformation associated with explosive eruptions at an andesitic volcano: Sakurajima volcano, Japan. In M. P. Ryan (Ed.), *Magma transport and storage*. John Wiley and Sons.

Japan Meteorological Agency. (2021). Report of 149th coordinating committee of prediction of volcanic eruption. Retrieved from https://www.data.jma.go.jp/svd/vois/data/tokyo/STOCK/kaisetsu/CCPVE/shiryo/149/149_2-1.pdf

Japan Meteorological Agency. (2022). Report of 151th coordinating committee of prediction of volcanic eruption. Retrieved from https://www.data.jma.go.jp/svd/vois/data/tokyo/STOCK/kaisetsu/CCPVE/shiryo/151/151_2-1.pdf

Japan Meteorological Agency. (2023). Sakurajima eruption observation table. Retrieved from https://www.jma-net.go.jp/kagoshima/vol/data/skr_exp_2023.html

Jokisch, H., Carstensen, K., Dau, W. D., Meyer, H. J., & Allkofer, O. C. (1979). Cosmic-ray muon spectrum up to 1 TeV at 75° zenith angle. *Physical Review D*, *19*(5), 1368–1372. https://doi.org/10.1103/PhysRevD.19.1368

Jones, K., Johnson, J., Aster, R., Kyle, P. R., & McIntosh, W. C. (2008). Infrasonic tracking of large bubble bursts and ash venting at Erebus volcano, Antarctica. *Journal of Volcanology and Geothermal Research*, *177*(3), 661–672. https://doi.org/10.1016/j.jvolgeores.2008.02.001

Kahl, M., Chakraborty, S., Costa, F., Pompilio, M., Liuzzo, M., & Viccaro, M. (2013). Compositionally zoned crystals and real-time degassing data reveal changes in magma transfer dynamics during the 2006 summit eruptive episodes of Mt. Etna. *Bulletin of Volcanology*, *75*(2), 692. https://doi.org/10.1007/s00445-013-0692-7

Kazahaya, R., Shinohara, H., Mori, T., Iguchi, M., & Yokoo, A. (2016). Pre-eruptive inflation caused by gas accumulation: Insight from detailed gas flux variation at Sakurajima volcano, Japan. *Geophysical Research Letters*, *43*(21), 11219–11225. https://doi.org/10.1002/2016GL070727

Konstantinou, K. I., & Schlindwein, V. (2002). Nature, wavefield properties and source mechanism of volcanic tremor: A review. *Journal of Volcanology and Geothermal Research*, *119*(1–4), 161–187. https://doi.org/10.1016/S0377-0273(02)00311-6

Lipari, P., & Stanev, T. (1991). Propagation of multi-TeV muons. *Physical Review D*, *44*(11), 3543–3554. https://doi.org/10.1103/PhysRevD.44.3543

Lo Presti, D., Gallo, G., Bonanno, D. L., Bonanno, G., Ferlito, C., La Rocca, P., et al. (2022). Three years of muography at Mount Etna, Italy: Results and interpretation. *Geophysical Monograph Series*, *270*, 93–108. https://doi.org/10.1002/9781119722748.ch7

Macedonio, G., Saracino, G., Ambrosino, F., Baccani, G., Bonechi, L., Bross, A., et al. (2022). Muography of the volcanic structure of the summit of Vesuvius. *Geophysical Monograph Series*, *270*, 123–136. https://doi.org/10.1002/9781119722748.ch9

Manga, M. (1996). Dynamics of drops in branched tubes. *Journal of Fluid Mechanics*, *315*, 105–117. https://doi.org/10.1017/S0022112096002352

Marchetti, E., Ripepe, M., Ulivieri, G., Caffo, S., & Privitera, E. (2009). Infrasonic evidences for branched conduit dynamics at Mt. Etna volcano, Italy. *Geophysical Research Letters*, *36*(19), L19308. https://doi.org/10.1029/2009GL040070

Miyagi, I., Shinohara, H., & Itoh, J. (2013). Variations of color and leachate contents of volcanic ashes from Sakurajima volcano, Japan. *Bulletin of the Volcanological Society of Japan*, *58*, 213–226. https://doi.org/10.18940/kazan.58.1_213

Muramatsu, D., Aizawa, K., Yokoo, A., Iguchi, M., & Tameguri, T. (2018). Estimation of vent radii from video recordings and infrasound data analysis: Implications for Vulcanian eruptions from Sakurajima volcano, Japan. *Geophysical Research Letters*, *45*(23), 12829–12836. https://doi.org/10.1029/2018GL079898

Nagahara, S., Miyamoto, S., Morishima, K., Nakano, T., Koyama, M., & Suzuki, Y. (2022). Three-dimensional density tomography determined from multi-directional muography of the Omuroyama scoria cone, Higashi-Izu monogenetic volcano field, Japan. *Bulletin of Volcanology*, *84*(10), 94. https://doi.org/10.1007/s00445-022-01596-y

Nagamine, K., Iwasaki, M., Shimomura, K., & Ishida, K. (1995). Method of probing inner-structure of geophysical substance with the horizontal cosmic-ray muons and possible application to volcanic eruption prediction. *Nuclear Instruments and Methods in Physics Research*, *356*(2–3), 585–595. https://doi.org/10.1016/0168-9002(94)01169-9

Natural Earth. (2024). Free vector and raster map data. Retrieved from https://www.naturalearthdata.com/
Nishiyama, R., Taketa, A., Miyamoto, S., & Kasahara, K. (2016). Monte Carlo simulation for background study of geophysical inspection with cosmic-ray muons. *Geophysical Journal International*, *206*(2), 1039–1050. https://doi.org/10.1093/gji/ggw191
Nishiyama, R., Tanaka, Y., Okubo, S., Oshima, H., Tanaka, H. K. M., & Maekawa, T. (2014). Integrated processing of muon radiography and gravity anomaly data toward the realization of high resolution 3D density structural analysis of volcanoes: Case study of Showa-Shinzan lava dome, Usu, Japan. *Journal of Geophysical Research: Solid Earth*, *119*(1), 699–710. https://doi.org/10.1002/2013JB010234
Nyitrai, G., Hamar, G., & Varga, D. (2021). Towards low gas consumption of muographic tracking detectors in field application. *Journal of Applied Physics*, *129*(24), 244901. https://doi.org/10.1063/5.0053984
Oláh, L. (2024a). 202405_JGRSE_2023JB028514_FigureData.zip [Dataset]. *Open Science Framework*. https://doi.org/10.17605/OSF.IO/TWS4J
Oláh, L. (2024b). 202312_JGRSE_2023JB028514_Software.zip [Software]. *Open Science Framework*. https://doi.org/10.17605/OSF.IO/TWS4J
Oláh, L., Balogh, S. J., Gera, Á. L., Hamar, G., Nyitrai, G., Tanaka, H. K. M., & Varga, D. (2019). MWPC-based muographic observation system for remote monitoring of active volcanoes. *Nuclear Instruments and Methods A*, *936*, 57–58. https://doi.org/10.1016/j.nima.2018.11.004
Oláh, L., Gallo, G., Hamar, G., Kamoshida, O., Leone, G., Llewellin, E. W., et al. (2023). Muon imaging of volcanic conduit explains link between eruption frequency and ground deformation. *Geophysical Research Letters*, *50*(2), e2022GL101170. https://doi.org/10.1029/2022GL101170
Oláh, L., & Tanaka, H. K. M. (2022). Muography of magma intrusion beneath the active craters of Sakurajima volcano. *Geophysical Monograph Series*, *270*, 109–122. https://doi.org/10.1002/9781119722748.ch8
Oláh, L., Tanaka, H. K. M., & Hamar, G. (2021). Muographic monitoring of hydrogeomorphic changes induced by post-eruptive lahars and erosion of Sakurajima volcano. *Scientific Reports*, *11*(1), 17729. https://doi.org/10.1038/s41598-021-96947-8
Oláh, L., Tanaka, H. K. M., Hamar, G., & Varga, D. (2019). Investigation of the limits of high-definition muography for observation of Mt Sakurajima. *Philosophical Transactions of the Royal Society A*, *377*(2137), 20180135. https://doi.org/10.1098/rsta.2018.0135
Oláh, L., Tanaka, H. K. M., Ohminato, T., Hamar, G., & Varga, D. (2019). Plug formation imaged beneath the active craters of Sakurajima volcano with muography. *Geophysical Research Letters*, *46*(17–18), 10417–10424. https://doi.org/10.1029/2019GL084784
Oláh, L., Tanaka, H. K. M., Ohminato, T., & Varga, D. (2018). High-definition and low-noise muography of the Sakurajima volcano with gaseous tracking detectors. *Scientific Reports*, *8*(1), 3207. https://doi.org/10.1038/s41598-018-21423-9
Oláh, L., Tanaka, H. K. M., & Varga, D. (2022). Muography: Exploring Earth's subsurface with elementary particles. *Geophysical Monograph Series*, *270*. https://doi.org/10.1002/9781119722748
Pioli, L., Azzopardi, B., & Cashman, K. (2009). Controls on the explosivity of scoria cone eruptions: Magma segregation at conduit junctions. *Journal of Volcanology and Geothermal Research*, *186*(3–4), 407–415. https://doi.org/10.1016/j.jvolgeores.2009.07.014
Portal, A., Labazuy, P., Lénat, J. F., Béné, S., Boivin, P., Busato, E., et al. (2013). Inner structure of the Puy de Dôme volcano: Cross-comparison of geophysical models (ERT, gravimetry, muon imaging). *Geoscientific Instrumentation, Methods and Data Systems*, *2*(1), 47–54. https://doi.org/10.5194/gi-2-47-2013
Ripepe, M., Marchetti, E., & Ulivieri, G. (2007). Infrasonic monitoring at Stromboli volcano during the 2003 effusive eruption: Insights on the explosive and degassing process of an open conduit system. *Journal of Geophysical Research: Solid Earth*, *112*(B9), B09207. https://doi.org/10.1029/2006JB004613
Salvatore, V., Silleni, A., Corneli, D., Taddeucci, J., Palladino, D. M., Sottili, G., et al. (2018). Parameterizing multi-vent activity at Stromboli volcano (Aeolian Islands, Italy). *Bulletin of Volcanology*, *80*(7), 64. https://doi.org/10.1007/s00445-018-1239-8
Schouten, D., & Lendru, P. (2018). Muon tomography applied to a dense uranium deposit at the McArtur River mine. *Journal of Geophysical Research: Solid Earth*, *123*, 8637–8652. https://doi.org/10.1029/2018JB015626
Simons, B. C., Cronin, S. J., Eccles, J. D., Bebbington, M. S., & Jolly, A. D. (2020). Spatiotemporal variations in eruption style, magnitude and vent morphology at Yasur volcano, Vanuatu: Insights into the conduit system. *Bulletin of Volcanology*, *82*(8), 59. https://doi.org/10.1007/s00445-020-01394-4
Spina, L., Taddeucci, J., Cannata, A., Sciotto, M., Del Bello, E., Scarlato, P., et al. (2017). Time-series analysis of fissure-fed multi-vent activity: A snapshot from the July 2014 eruption of Etna volcano (Italy). *Bulletin of Volcanology*, *79*(7), 51. https://doi.org/10.1007/s00445-017-1132-x
Tanaka, H. K. M. (2019). Japanese volcanoes visualized with muography. *Philosophical Transactions of the Royal Society A*, *377*(2137), 20180142. https://doi.org/10.1098/rsta.2018.0142
Tanaka, H. K. M. (2020). Development of the muographic tephra deposit monitoring system. *Scientific Reports*, *10*(1), 14820. https://doi.org/10.1038/s41598-020-71902-1
Tanaka, H. K. M., Bozza, C., Bross, A., Cantoni, E., Catalano, O., Cerretto, G., et al. (2023). Muography. *Nature Reviews Methods Primers*, *3*(1), 88. https://doi.org/10.1038/s43586-023-00270-7
Tanaka, H. K. M., Kusagaya, T., & Shinohara, H. (2014). Radiographic visualization of magma dynamics in an erupting volcano. *Nature Communications*, *5*(1), 3381. https://doi.org/10.1038/ncomms4381
Tanaka, H. K. M., Nakano, T., Takahashi, S., Yoshida, J., Takeo, M., Oikawa, J., et al. (2007). High resolution imaging in the inhomogeneous crust with cosmic-ray muon radiography: The density structure below the volcanic crater floor of Mt. Asama, Japan. *Earth and Planetary Science Letters*, *263*(1–2), 104–113. https://doi.org/10.1016/j.epsl.2007.09.001
Tanaka, H. K. M., Taira, H., Uchida, T., Tanaka, M., Takeo, M., Ohminato, T., et al. (2010). Three-dimensional computational axial tomography scan of a volcano with cosmic ray muon radiography. *Journal of Geophysical Research: Solid Earth*, *115*(B12), B12332. https://doi.org/10.1029/2010JB007677
Tang, A., Horton-Smith, G., Kudryavtsev, V. A., & Tonazzo, A. (2006). Muon simulations for Super-Kamiokande, KamLAND, and CHOOZ. *Physical Review D*, *74*(5), 053007. https://doi.org/10.1103/PhysRevD.74.053007
The European Space Agency (ESA). (2023). SAR instrument. Retrieved from https://sentinels.copernicus.eu/web/sentinel/technical-guides/sentinel-1-sar/sar-instrument
Tioukov, V., Giudicepietro, F., Macedonio, G., Calvari, S., Di Traglia, F., Fornaciai, A., & Favalli, M. (2022). Structure of the shallow supply system at Stromboli volcano, Italy, through integration of muography, digital elevation models, seismicity, and ground deformation data. *Geophysical Monograph Series*, *270*, 75–91. https://doi.org/10.1002/9781119722748.ch6
Uhira, K., & Takeo, M. (1994). The source of explosive eruptions of Sakurajima volcano, Japan. *Journal of Geophysical Research: Solid Earth*, *99*(B9), 17775–17789. https://doi.org/10.1029/94JB00990
Varga, D., Hamar, G., Balogh, S., Gera, A., Nyitrai, G., & Surányi, G. (2022). Construction and readout systems for gaseous muography detectors. *Journal of Advanced Instrumentation in Science*, *2022*. JAIS-307. https://doi.org/10.31526/jais.2022.307
Varga, D., Hamar, G., Nyitrai, G., & Oláh, L. (2016). High efficiency gaseous tracking detectors for cosmic muon radiography. *Advances in High Energy Physics*, *2016*, 1962317. https://doi.org/10.1155/2016/1962317

Varga, D., Nyitrai, G., Hamar, G., Galgóczi, G., Oláh, L., Tanaka, H., & Ohminato, T. (2020). Detector developments for high performance muography applications. *Nuclear Instruments and Methods in Physics Research*, *958*, 162236. https://doi.org/10.1016/j.nima.2019.05.077

Watt, S. F. L., Mather, T. A., & Pyle, D. M. (2007). Vulcanian explosion cycles: Patterns and predictability. *Geology*, *35*(9), 839–842. https://doi.org/10.1130/G23562A.1

Yokoo, A., Iguchi, M., Tameguri, T., & Yamamoto, K. (2013). Processes prior to outbursts of Vulcanian eruption at Showa crater of Sakurajima volcano. *Bulletin of the Volcanological Society of Japan*, *58*, 163–181. https://doi.org/10.18940/kazan.58.1_163

Zuccarello, L., De Angelis, S., Minio, V., Saccorotti, G., Bean, C. J., Paratore, M., & Ibanez, J. M. (2022). Volcanic tremor tracks changes in multi-vent activity at Mt. Etna, Italy: Evidence from analyses of seismic array data. *Geophysical Research Letters*, *49*(22), e2022GL100056. https://doi.org/10.1029/2022GL100056